JGR Atmospheres

RESEARCH ARTICLE
10.1029/2021JD034644

Identifying Outflow Regions of North American Monsoon Anticyclone-Mediated Meridional Transport of Convectively Influenced Air Masses in the Lower Stratosphere

C. E. Clapp[1], J. B. Smith[1], K. M. Bedka[2], and J. G. Anderson[1,3,4]

[1]Harvard John A. Paulson School of Engineering and Applied Sciences, Harvard University, Cambridge, MA, USA, [2]NASA Langley Research Center, Hampton, VA, USA, [3]Department of Chemistry and Chemical Biology, Harvard University, Cambridge, MA, USA, [4]Department of Earth and Planetary Sciences, Harvard University, Cambridge, MA, USA

Key Points:

- Trajectory analysis of overshooting tops identified by GOES satellite is used to evaluate meridional transport of cross-tropopause convective outflow
- The North American monsoon anticyclone (NAMA) circulation and its seasonality dictates the extent of meridional transport that occurs in the lower stratosphere
- During July and August, when the NAMA is strongest, the average convectively influenced air mass is transported 22.0° northward

Correspondence to:
C. E. Clapp,
cclapp@fas.harvard.edu

Citation:
Clapp, C. E., Smith, J. B., Bedka, K. M., & Anderson, J. G. (2021). Identifying outflow regions of North American monsoon anticyclone-mediated meridional transport of convectively influenced air masses in the lower stratosphere. *Journal of Geophysical Research: Atmospheres*, *126*, e2021JD034644. https://doi.org/10.1029/2021JD034644

Received 22 JAN 2021
Accepted 29 APR 2021

Abstract We analyzed the effect of the North American monsoon anticyclone (NAMA) on the meridional transport of summertime cross-tropopause convective outflow by applying a trajectory analysis to a climatology of convective overshooting tops (OTs) identified in GOES satellite images, which covers the domain from 29°S to 68°N and from 205°W to 1.25°W for the time period of May to September, 2013. From this analysis, we identify seasonal development of geographically distinct outflow regions of convectively influenced air masses (CIAMs) from the NAMA circulation to the global stratosphere and quantify the associated meridional displacement of CIAMs. We find that prior to the development of the NAMA, the majority of CIAMs exit the study area in a southeastern region between 5°N and 35°N at 45°W (75.5% in May). During July and August, when the NAMA is strongest, two additional outflow regions develop that constitute the majority of outflow: 68.1% in a northeastern region between 35°N and 60°N at 45°W and 13.4% in a southwestern region between 5°N and 35°N at 145°W. The shift in the location of most CIAM outflow from the pre-NAMA southeastern region to NAMA-dependent northeastern and southwestern regions corresponds to a change in average meridional displacement of CIAMs from 3.3° northward in May to 24.5° northward in July and August. Meridional transport of CIAMs through persistent outflow regions from the NAMA circulation to the global stratosphere has the potential to impact global stratospheric composition beyond convective source regions.

Plain Language Summary We analyze the seasonal and regional variability of the transport of convection that has reached the lower stratosphere (an exceptional height) over North America from May to September within the large-scale but transient summertime anticyclone over North America. Overshooting convection that has reached the lower stratosphere is identified using infrared and visible satellite imagery. We simulate the circulation of the convectively influenced air to track its motion throughout the season from its initial position until it exits the study region and enters the global stratosphere. We find that the development of the anticyclone dictates through which of three outflow regions the majority of convectively influence air masses exit. Prior to the anticyclone's development most air masses exit through southeastern region over the Atlantic Ocean below 35°N. When the anticyclone is strongest, during July and August, most air masses exit through a northeastern region over the Atlantic Ocean above 35°N and through a southwestern region over the Pacific Ocean. During July and August the average air mass is transported 24.5° northward from its initial position. This transport may influence the global stratospheric water budget, as well as transport pollutants from this region into the global stratosphere.

1. Introduction

Cross-tropopause convection within the North American monsoon anticyclone (NAMA) has been shown to influence the composition of the upper troposphere and lower stratosphere (UTLS) over North America during the boreal summer, but its overall effects are poorly understood. Moreover, the NAMA is associated with a local boreal summer water vapor maximum and ozone minimum (Ploeger, Günther, et al., 2013; Randel, Zhang, & Fu, 2015; Schwartz et al., 2013). The composition of the UTLS is significant because of

these radiatively important gases (water vapor and ozone) and because of the potential impacts on ozone chemistry. The distributions of water vapor (Riese et al., 2012; Solomon, Rosenlof, et al., 2010) and ozone (Kuilman et al., 2020; Nowack et al., 2018; Shine et al., 2003; Xia et al., 2018) in the UTLS have been shown to strongly influence radiative forcing and surface temperatures. Further, water vapor mixing ratios, as well as those of other convectively influenced chemical species, in the UTLS have the potential to kinetically favor the heterogeneous chemistry that drives halogen catalyzed ozone loss (Anderson & Clapp, 2018; Anderson, Weisenstein, et al., 2017; Anderson, Wilmouth, et al., 2012; Liang et al., 2014; Robrecht et al., 2019; Schoeberl et al., 2020; Schwartz et al., 2013; Sinnhuber & Meul, 2015; Solomon, Kinnison, et al., 2016; Wales et al., 2018). To begin to quantify the influence of cross-tropopause convection on UTLS composition, we utilize a climatology of satellite identified deep convection to evaluate meridional transport of convectively influenced air masses (CIAMs) and outflow regions of the NAMA stratospheric circulation to the global stratosphere.

Cross-tropopause convection has been shown to rapidly transport boundary layer air and entrained tropospheric air, environmental air mixed into convective updrafts, into the lower stratosphere by in situ measurements (Bucci et al., 2020; Corti et al., 2008; de Reus et al., 2009; Gettelman et al., 2004; Hegglin et al., 2004; Herman et al., 2017; Khaykin, Pommereau, Korshunov, et al., 2009; Khaykin, Pommereau, Riviere, et al., 2016; Pittman et al., 2007; Poulida et al., 1996; Ray et al., 2004; Sargent et al., 2014; Sayres et al., 2010; Smith et al., 2017; Weinstock et al., 2007), satellite observations (Eguchi et al., 2016; Hanisco et al., 2007; Homeyer, 2014; Homeyer et al., 2017; Iwasaki, Shibata, Nakamoto, et al., 2010; Iwasaki, Shibata, Okamoto, et al., 2012; Randel, Moyer, et al., 2012), and modeling studies (Hassim & Lane, 2010; Li et al., 2005; Phoenix, Homeyer, & Barth, 2017; Qu et al., 2020; Sang et al., 2018; P. K. Wang et al., 2011). Convective transport bypasses the dominant global scale troposphere-to-stratosphere transport associated with the Brewer-Dobson circulation of slow ascent of air in the tropics across the tropical tropopause followed by meridional transport. As a result of its rapid nature, the cross-tropopause convective transport mechanism impacts the composition of the UTLS by introducing air masses chemically distinct from air transported by the slow ascent of the Brewer-Dobson cycle. This convectively influenced chemically distinct air has been observed in situ in the UTLS over North America including perturbations to water vapor, ozone, and other tracers (Gettelman et al., 2004; Herman et al., 2017; Li et al., 2005; Pittman et al., 2007; Ray et al., 2004; Smith et al., 2017; Weinstock et al., 2007). Moreover, the NAMA has been shown to be the region of greatest cross-tropopause convective moistening by a global analysis of both satellite and in situ observations of elevated stratospheric water vapor (Jensen et al., 2020; Werner et al., 2020) and by satellite observations of deuterated water, HDO (Hanisco et al., 2007; Randel, Moyer, et al., 2012). Model simulations of cross-tropopause convection reproduce these observations of convective UTLS compositional influence including both the upward transport of tropospheric air and the less understood downward mixing of stratospheric air by dynamical processes, including gravity wave breaking and mass conservation driven subsidence, globally (Frey et al., 2015; Sang et al., 2018), and over North America (Homeyer et al., 2017; Phoenix, Homeyer, & Barth, 2017; Phoenix, Homeyer, Barth, & Trier, 2020; Qu et al., 2020).

The interaction between cross-tropopause convection and the larger NAMA circulation controls the ultimate impact on stratospheric composition through the redistribution of the convective outflow. The NAMA has been shown to transport convectively influenced air masses far from the geographic source region in trajectory analyses of in situ observations of trace species including water vapor, carbon monoxide, and carbon dioxide (Li et al., 2005; Gettelman et al., 2004; Herman et al., 2017; Pittman et al., 2007; Randel, Moyer, et al., 2012; Ray et al., 2004; Smith et al., 2017; Weinstock et al., 2007), and in modeling studies of water vapor (Nützel et al., 2019; Ploeger, Günther, et al., 2013; Poshyvailo et al., 2018) and of potential vorticity streamers (Kunz et al., 2015). Further, a study of satellite measured water vapor and radar observed convection occurring over the continental US has demonstrated the importance of the NAMA circulation mediating the convective hydration of the lower stratosphere (Yu et al., 2020). Several trajectory analyses of satellite identified cross-tropopause convection have shown that the NAMA circulation contains outflow over North America with significant contributions from convection over the Sierra Madres and the tropics (Clapp et al., 2019; X. Wang et al., 2021). Finally, the NAM has also been shown in a modeling study to have a transport efficiency of air into the stratosphere comparable to the efficiency of the tropics, though less than that of the Asian monsoon (Yan et al., 2019).

While the transport of boundary layer air, including halogen very short-lived species (VSLS), into the global lower stratosphere by deep convection and through monsoon circulation has been studied in the Asian monsoon using climate models (Fadnavis et al., 2018; Wu et al., 2020) and trajectory analyses (Fiehn et al., 2017; Garny & Randel, 2016; Vogel, Günther, Müller, Grooß, Hoor, et al., 2014; Vogel, Müller, et al., 2019), the potential transport pathways of CIAMS through the NAMA to the global lower stratosphere is not well understood. Chemical-transport studies that accurately reproduce satellite observations of the seasonal summer stratospheric water vapor maximum over the Asian monsoon but do not capture the NAMA maximum exemplify this discrepancy (Nützel et al., 2019; Ploeger, Günther, et al., 2013; Poshyvailo et al., 2018).

In this work, we assess net meridional transport of CIAMs within the NAMA circulation, and identify specific outflow regions of CIAMs from the anticyclone to the global stratosphere. To accomplish this we performed a trajectory analysis of "overshooting tops" (OTs) identified using GOES satellite images (Bedka & Khlopenkov, 2016) in the May to September of 2013 time period and constructed a climatology of outflow from the NAMA region. OTs, deep convective updrafts that penetrate the cirrus anvil and local tropopause, were used to indicate cross-tropopause convection, although they do not independently verify that irreversible transport from the troposphere to stratosphere occurred. The forward trajectories initialized at each OT, were evaluated using Modern-Era Retrospective Reanalysis for Research and Applications, Version 2 (MERRA-2) winds to simulate the effect of the NAMA. From this work (a) the effect of the NAMA circulation on the meridional transport of CIAMs and its seasonal, geographic, and altitude trends are quantified and (b) the dominant outflow regions from the NAMA into the global lower stratosphere are identified and their seasonal evolution is evaluated.

2. Data and Methods

The present analysis of potential cross-tropopause transport by deep convection and subsequent transport by the NAMA was conducted by tracking trajectories of CIAMs, which are described in more detail below. The CIAMs were identified using an OT climatology derived from GOES satellite images and the trajectories tracking these parcels from their initial source region through the NAMA and out to the global stratosphere were driven using MERRA-2 winds (see also Clapp et al. [2019] for a description of both these products).

The OT climatology, derived from GOES data, represents a hemispheric record of convection with coverage from 29°S to 68°N and from 205°W to 1.25°W, which we define as our study domain. OTs are algorithmically identified using multispectral imagery from GOES-13 and 15 (Bedka & Khlopenkov, 2016), and the product was used previously in Clapp et al. (2019). Updrafts that overshoot their anvil altitude but do not reach the tropopause are not included in this study. To represent the subsequent movement of convectively influenced air parcels, a three-dimensional trajectory analysis was performed for each OT for the time period from May 1, 2013 to September 30, 2013. The trajectories were initialized using the latitude, longitude, time, pressure, and potential temperature of the cloud top of each observed OT (1 trajectory per OT) provided by the OT climatology. Only OTs with detection probability ratings (as determined by the temperature differences between the OT and the anvil, tropopause, and local level of neutral buoyancy) greater than or equal to 0.9 were used in this analysis. Here, the tropopause was determined by the MERRA-2 tropopause analysis which is based on a combination of the WMO definition of the primary lapse rate tropopause and equivalent potential vorticity (Gelaro et al., 2017). The detection probability threshold detected ∼50% of human-identified OTs randomly sampled throughout the world (Bedka & Khlopenkov, 2016). At this rating, the false detection rate was determined to be ∼10%, and these errant detections were typically found in close proximity to actual OT regions, so inclusion of these samples in the trajectory analysis does not adversely affect the results. The Bedka and Khlopenkov (2016) OT identification method (which performs best in the detection of OTs associated with storms with strong updrafts) is a conservative methodology that underpredicts OTs allowing for high confidence in the OTs that are detected. The potential temperature of each OT was derived from the OT IR temperature and pressure derived from the OT height and MERRA-2 (Gelaro et al., 2017) reanalysis, using the method of Griffin et al. (2016).

Trajectory wind fields were taken from the MERRA-2 reanalysis, available at 0.5° × 0.625° spatial resolution and 3 h temporal resolution. The trajectory calculations of the CIAMs utilize a three-dimensional kinematic fourth order Runge-Kutta method with a time step of 3 h (Clapp et al., 2019). Trajectories initialized at the

location and time of individual OTs were calculated until the trajectory left the bounding box of the study domain, 29°S to 68°N and 205°W to 1.25°W, with a vertical extent from 350 to 550 K. Three-hundred fifty Kelvin was selected as a lower bound for the purposes of the trajectory calculations, beyond which the CIAM is considered to have returned to the troposphere. In the following discussion we focus on the 370 and 400 K levels to differentiate between the more frequent "shallow" cross-tropopause convection, and the less frequent "deep" cross-tropopause convection, which have different geographic and seasonal source distributions. For example, when considering "deep" cross-tropopause convection the central US becomes a significant source region, particularly in May, June, and August (Clapp et al., 2019; Cooney et al., 2018). When considering "shallow" cross-tropopause convection, however, the tropics and the Sierra Madre regions are more important (Clapp et al., 2019).

The use of MERRA-2 reanalysis winds for trajectory calculation is limited by the native resolution of the reanalysis (0.5° × 0.625°), and by the influence that the convective overshoots may have had on stratospheric winds at the point of trajectory initiation that is not represented by the reanalysis. Further, despite the relatively high spatial resolution, the coarseness of the temporal resolution of the MERRA-2 reanalysis wind fields is also limiting factor that can lead to errors in trajectory calculation due to sampling errors arising from the undersampling of the wind fields in time relative to space (Bowman et al., 2013; Hoffmann et al., 2019; Stohl et al., 1995). Errors in identifying the OT altitude and potential temperature from which to initiate the trajectory are also a limitation. The large number of trajectories used, however, should minimize the effect of error in individual trajectories, and is sufficient to evaluate large-scale trends in transport and outflow.

The OT distribution and CIAM trajectory climatology do not represent a complete budget of cross-tropopause convection occurring in the study region and over the time period considered. This is because the GOES OT data were acquired every half hour while the average lifetime of an OT is several minutes (Bedka & Khlopenkov, 2016). Consequently, the OT data set used in this study represents a small percentage of the total number of OTs that occurred and should not be used to estimate total convective outflow. The OT data set, however, is still valid for analyzing large-scale transport trends and distributions because the consistent and frequent sampling, the long time period under study, and the large region of interest retain the major features of OT frequency, depth, and geographic distribution.

To restrict the analysis to CIAMs influenced by the NAMA, only CIAMs with trajectories that passed through the NAMA region (defined as 17.5°N to 45°N and 122.5°W to 85°W, see Figure 1) were considered. This region, though representative of the NAMA geographic position, is intentionally larger than the instantaneous geographic extent of the NAMA (as defined by a closed contour of the Montgomery streamfunction at any given potential temperature level) to account for the instability of the NAMA in both position and strength over time. Using a larger representative region ensured consideration of all CIAMs likely influenced by the anticyclonic circulation during the entire season. CIAM trajectories were considered to have exited the area of NAMA influence once they permanently crossed an outer boundary (defined as 6°N to 70°N and 145°W to 45°W, see Figure 1), that is, the trajectory did not re-enter the outer boundary before leaving the larger study area (29°S to 68°N and 205°W to 1.25°W). The point and time at which the CIAM trajectory crossed this outer boundary is considered the outflow event from the NAMA circulation region into the global lower stratosphere for the purposes of identifying seasonal outflow regions to the global stratosphere. As CIAM trajectories were simulated until leaving the larger study region all outflow events occurring from May to September were captured. Further, to ensure that only CIAMs that had reached the stratosphere were included in the analysis, trajectories that were below the local tropopause, determined using the WMO lapse rate tropopause definition and MERRA-2 meteorological fields, at the point of crossing the outer boundary were not considered. In total, 207,691 CIAMs are included in the study.

3. Results

3.1. Seasonality of the NAMA and of Cross-Tropopause Convection

In order to distinguish transport of CIAMs through the NAMA circulation from transport via the background stratospheric flow, we first analyze the seasonally dependent properties of NAMA location and strength, independent from CIAM trajectories. The location and strength of the NAMA is quantified using

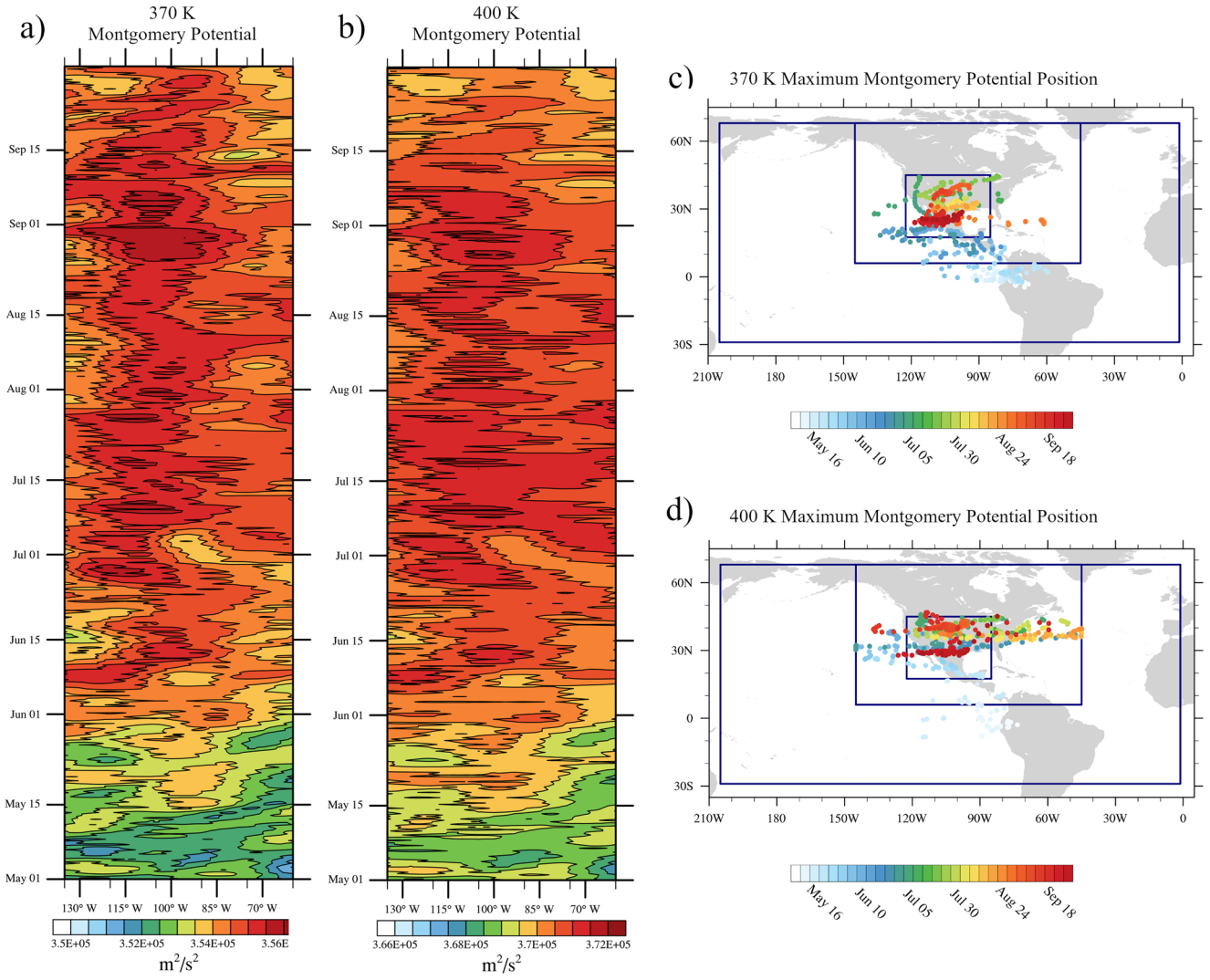

Figure 1. The seasonal development of the NAMA (North American monsoon Anticyclone) shown using the Montgomery potential (streamfunction on potential temperature surfaces) calculated from MERRA-2 reanalysis data at 370 and 400 K. Panels (a and b) show the Hovmöller diagram of Montgomery potential calculated as an average between 17.5°N and 45°N at 370 and 400 K respectively. Panels (c and d) show the seasonal evolution of the geographic location of the maximum Montgomery potential (calculated averaging over 2.5° × 3.125° bins) between 50°W and 140°W at 370 and 400 K, respectively. The innermost box in panels (c and d) depicts the NAMA-filtering region, the intermediate box depicts the outflow boundary of the study region, and the outermost box depicts the study region, which is the geographic extent of the OT data set (see the Methods section for more details).

the maximum Montgomery potential over North America (defined between 50°W and 140°W) at various potential temperatures in the UTLS. Montgomery potential, defined as:

$$M = \Phi + C_p T$$

where Φ is the geopotential, C_p is the specific heat of air at constant pressure, and T is the temperature, is the streamfunction for geostrophic wind on isentropic surfaces. Montgomery potential is the appropriate streamfunction for the analysis of circulation on isentropic surfaces, and has been used to evaluate anticyclones using potential temperature as the vertical coordinate in prior studies for the Asian monsoon anticyclone (Ploeger, Gottschling, et al., 2015; Popovic & Plumb, 2001; Santee et al., 2017), and the NAMA (Clapp et al., 2019).

Figure 1 illustrates the seasonal cycle of the NAMA during the study period to identify when it is expected to have the greatest influence. Figures 1a and 1b show Hovmöller diagrams of the Montgomery potential averaged between 17.5°N and 45°N from May to September of 2013 for 370 and 400 K, respectively.

The geographic position of the daily running mean maximum Montgomery potential over North America during the same time period at both levels is also shown in Figures 1c and 1d. The Hovmöller diagrams show the absence of the NAMA in May (Diem et al., 2013; Geil et al., 2013; Vera et al., 2006), its initiation in June, and strengthening in July that is maintained through August particularly between 120°W and 90°W. Comparison of the Montgomery potential at 370 and 400 K reveals the vertical structure of the NAMA, an increase in strength with altitude (the average value for the months of June, July, and August was 3.55×10^5 m^2/s^2 at 370 K in Figure 1a and 3.71×10^5 m^2/s^2 at 400 K in Figure 1b) and a geographic shift northward (the maximum values range between 0.4°N and 44.6°N with an average of 27.7°N for the months of June, July, and August at 370 K in Figure 1c and between 29.8°N and 45.9°N with an average of 37.4°N for the same time period at 400 K in Figure 1d).

The development of the NAMA throughout the summer has a strong impact on the CIAM trajectories. Figure 2 shows the monthly average Montgomery streamfunction at 370 K for the months of May to September. Overlaid on the Montgomery streamfunction contour plots are a subset of CIAM trajectories (markers) included to illustrate the influence of the NAMA circulation. The color of the marker indicates the date of the CIAM trajectory initiation. The NAMA-driven transition from a largely zonal stratospheric flow early in the season to a closed circulation, though intermittent, that is strongest in August is apparent in both streamfunctions and trajectories. In May and June, the Montgomery streamfunction shows zonal flow throughout the domain, although in June the 355,000 m^2/s^2 contour is beginning to show a distortion. In July, August, and September however, anticyclonic circulation is apparent. For example, the 355,000 m^2/s^2 contour becomes closed in July and remains so through August. Similarly, the sample trajectories shown transition from largely zonal paths in May to circulations through the NAMA region in the latter three months.

As a consequence of this seasonality of the NAMA, its impact on the meridional transport of CIAMs and the development of distinct outflow regions is expected to manifest beginning in late June and be prominent through September with a maximum in August. Further, the increasing strength of the NAMA circulation with altitude through the UTLS also suggests it exerts a more consistent influence on CIAM outflow at 400 K and above.

It is also important to consider the underlying geographic distribution of CIAM initial locations in order to account for seasonal trends in cross-tropopause convection that may contribute to changes in the locations of CIAM outflow across the outer boundary. Figure 3 shows the monthly distributions of all CIAMs considered in this study for the months of May to September. The seasonal dependence of the relative importance of different source regions is apparent. Most notably, the central US has its highest contribution of cross-tropopause convection in May and June relative to other regions. In contrast, the Sierra Madre region grows in convective contribution through July and August, and becomes dominant in September. The tropical Pacific region is a significant source in all months. Further, the frequency of cross-tropopause convection grows throughout the summer, reaching a maximum in August (69,353 CIAMs). These trends largely follow the conclusions of Clapp et al. (2019).

The interaction of the seasonal geographic distribution of CIAM initial locations with the seasonal development of the NAMA results in a changing population of "active" CIAMs (CIAMs that have not yet permanently left the outflow boundary) as the rate of initial cross-tropopause convection, the rate of CIAM outflow, and the duration of entrapment within the NAMA circulation vary with time. Figure 4a shows the number of CIAMs initiated per day, the number of CIAMs that outflow per day, and the resulting number of "active" CIAMs, as a function of time at a daily resolution. The population of "active" CIAMs grows to a maximum in August, before declining through September. This trend shows the effects of both the seasonality of cross-tropopause convection, and of the development of NAMA circulation. The increasing frequency of cross-tropopause convection from May to September (shown by the increasing CIAM initiation) directly adds to the number of "active" CIAMs, while the increasing strength of the NAMA circulation, entraps CIAMs and delays outflow, resulting in a greater accumulation of "active" CIAMs. This entrapment is visible in Figures 4b and 4c which show histograms of the distributions of CIAM trajectory duration, from initiation to outflow, and of the NAMA residence time, the total time a CIAM trajectory was within the NAMA region (17.5°N-45°N and 122.5°W-85°W), subdivided by month of initiation. For example, of the CIAM trajectories that had a 5 day duration, 559 (17.8%) were initiated in May and 1,212 (38.6%) were initiated in August, while of the CIAM trajectories that had a 20 day duration, 114 (5.0%) were initiated in May

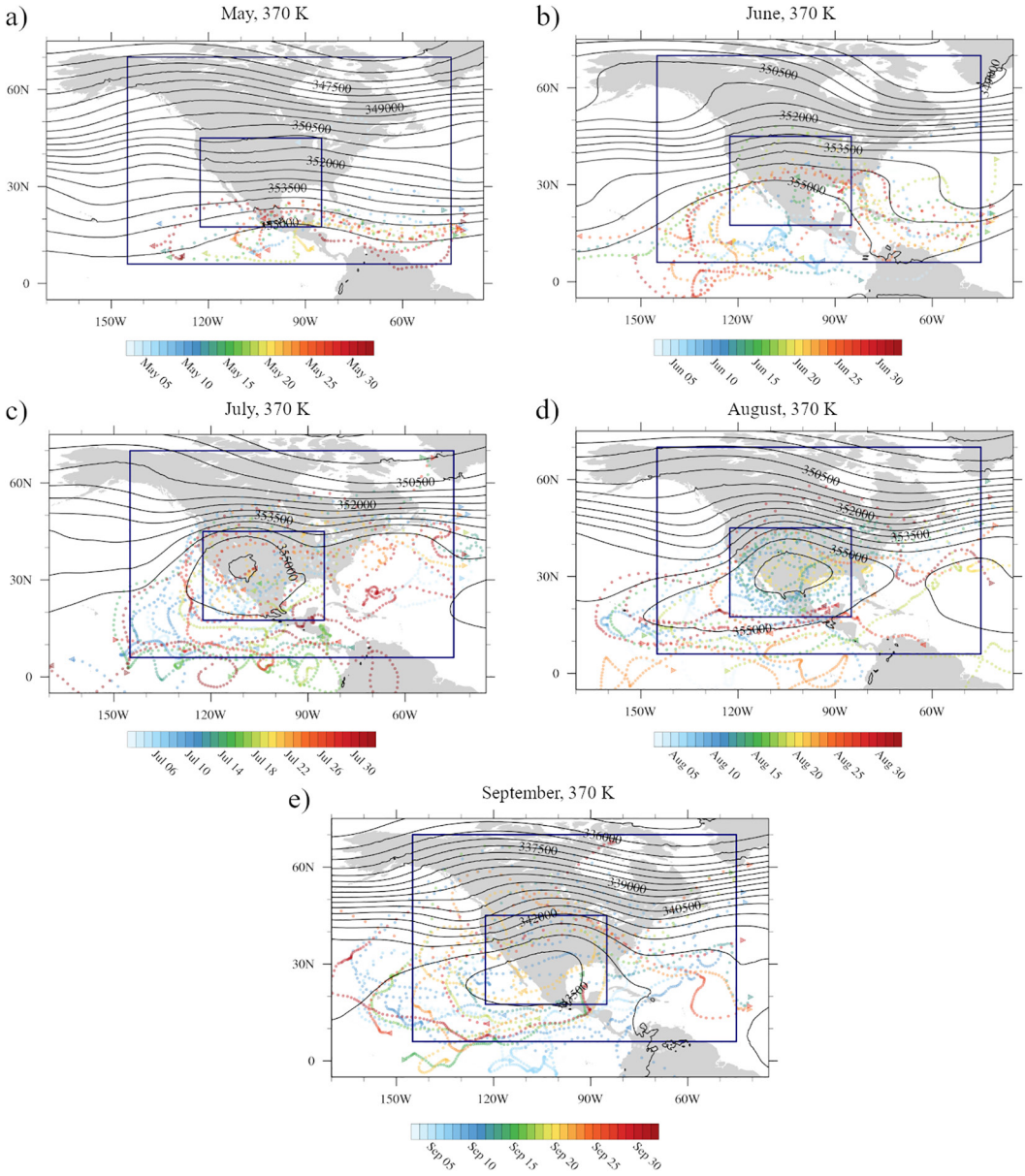

Figure 2. The influence of the NAMA circulation on convectively influenced air mass (CIAM) trajectories shown by the monthly average Montgomery potential at 370 K for the months of May to September in contours with a subset of CIAM trajectories overlaid in markers. The CIAM trajectories are a subset of those initialized within the month of interest at 370 K with the date of trajectory initialization indicated by the color of the markers. The left-pointing triangle indicates the location of the initial OT, the right-pointing triangle indicates the location of outflow, and the circles the body of the trajectory. Progression from one marker to the next follows the 3-h time step of the trajectory.

and 861 (37.4%) were initiated in August. Similarly, the months of July, August, and September contribute most of the CIAM trajectories that had a NAMA residence time greater than 5 days.

3.2. NAMA-Mediated Meridional Transport of CIAMs

In order to quantify the geographic distribution of CIAM outflow and identify any regions of consistent outflow and their seasonality, Figure 5 shows the evolution of the latitudinal distribution of CIAM outflow at the eastern and western boundaries of the study region (45°W and 145°W, respectively) over time for all CIAMs. In Figures 5a and 5b, outflow values are presented as a percentage of total outflow on each day

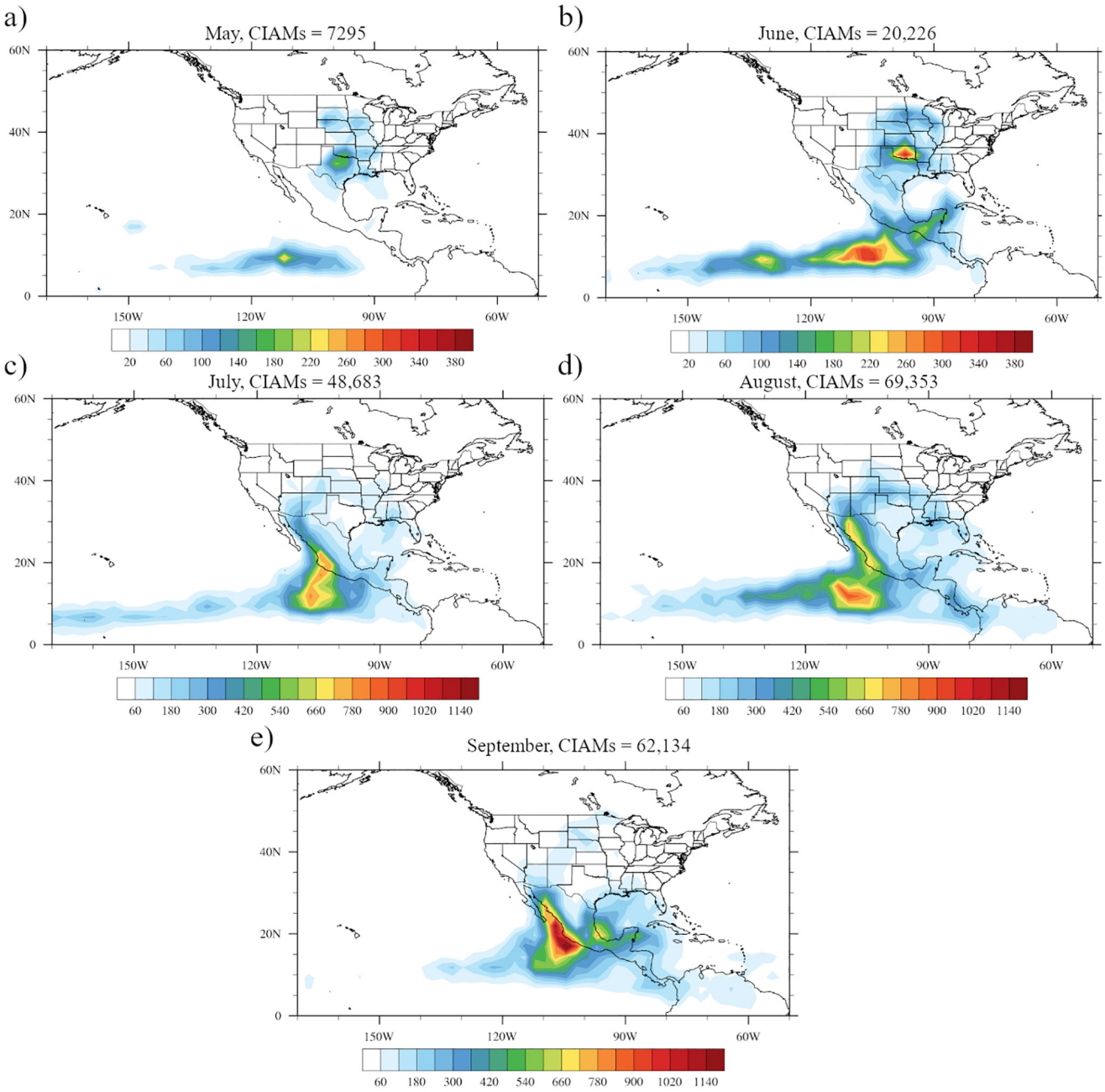

Figure 3. The seasonal development of the geographic distribution of all cross-tropopause convection included in this study shown by the CIAM initial locations binned at 2.5° × 2.5° for the months of May to September. The total number of CIAMs initialized within each month is indicated above each plot. Note the change in contour levels between panels (a and b) and panels (c–e).

across the boundary of interest to remove the effect of the seasonal changes in total cross-tropopause convection. To ensure that changes in the latitudinal distribution of outflow are not simply reflecting seasonal changes in the distribution of initial latitude of cross-tropopause convection within a context of hypothetical background zonal winds, Figures 5d and 5e show the ratio of percent CIAM outflow across the western and eastern boundary respectively at a given latitude to percent initial cross-tropopause convection at that latitude, for each daily mean value:

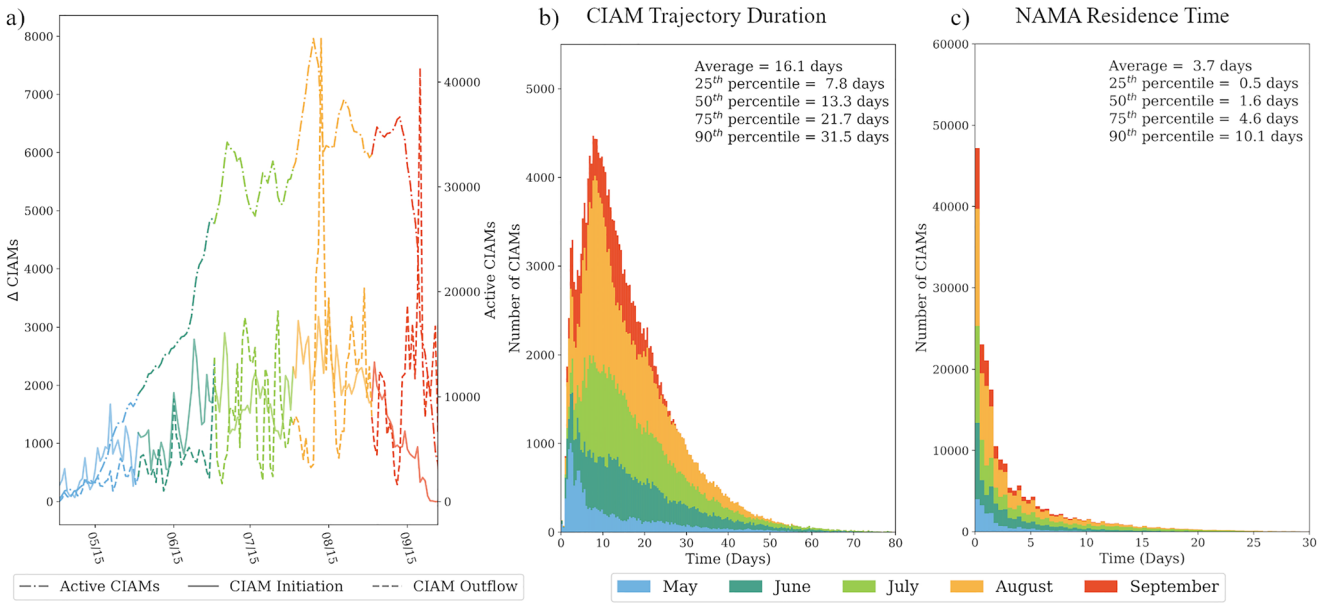

Figure 4. The seasonal change in temporal duration of CIAM trajectories and their entrapment within the NAMA region. Panel (a) shows the number of "active" CIAMs, those that have not yet permanently left the outflow boundary (dash-dot line, right axis), the number of CIAMs initialized (solid line, left axis), and the number of CIAM outflow (dashed line, left axis) as a function of time at a daily resolution with the color of the line indicating the month. Panel (b) shows a histogram of the duration of all CIAM trajectories binned in 10 h intervals. The color divisions of each bin indicates the fractional contribution of each month to that bin. For example, of the CIAMs in the duration bin of 240–250 h, May contributed 206 (5.0%), June contributed 641 (15.5%), July contributed 1,046 (25.4%), August contributed 1,656 (40.2%), and September contributed 575 (13.9%). Panel (c) shows a histogram of the NAMA residence time of all CIAM trajectories binned in 1 day intervals. The color of each bin indicates the fractional contribution of each month to that bin.

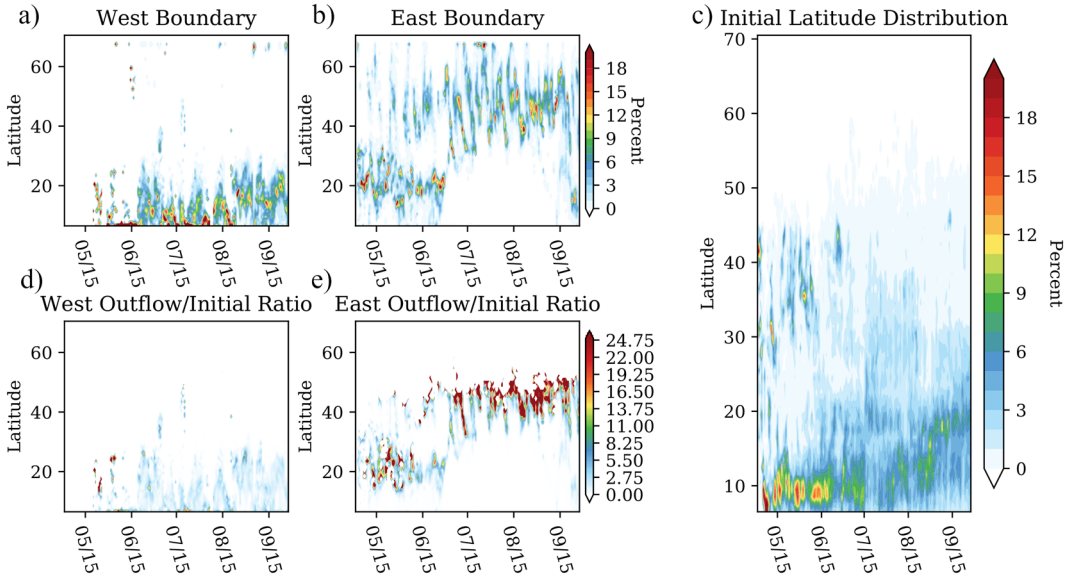

Figure 5. The seasonal development of the latitudinal distribution of CIAM outflow across the eastern (45°W) and western (145°W) boundaries of the study region. Panels (a and b) show the percent of CIAM outflow occurring at each latitude (as binned by 1°) of total outflow across the boundary of interest as a function of time. Panel (c) shows the percent latitude distribution of the initial latitude (1° bins) of all CIAMs considered as a function of time. Panels (d and e) show the ratio of percent CIAM outflow at a given latitude to percent CIAMs initialized at that latitude (1° bins) as a function of time.

$$R_{\text{boundary-latitude}} = \frac{\%\ \text{Outflow}_{\text{boundary-latitude}}}{\%\ \text{Initial Convection}_{\text{latitude}}}$$

At latitudes where more CIAM outflow occurs than initial cross-tropopause convection the ratio is greater than one. If, for example, the northward shift in outflow along the east boundary over time (Figure 5b) was a result of seasonal changes in the underlying distribution of cross-tropopause convection being advected eastward in a zonal flow (that is to say, if the distribution shown in Figure 5c mimicked Figure 5b), then the ratios in Figure 5e would be near one at all latitudes. High ratios indicate that the CIAM outflow at a given latitude is not matched by initial cross-tropopause convection at that given latitude. Therefore much of the CIAM outflow at that latitude was transported meridionally from its initial position and is not a result of purely zonal flow. Figure 5c shows the underlying percent latitude distribution of initial cross-tropopause convection.

The influence of the NAMA on outflow is most visible along the eastern boundary (Figure 5b). In May, prior to the development of the NAMA (see Figure 1) the majority of convective outflow (on average 83.8%) occurs in a southern band between approximately 5°N and 35°N. Beginning in late June coincident with the initiation of the NAMA, however, a consistent northern outflow zone appears between 35°N and 60°N. This northern band becomes the dominant outflow region (on average 91.2%) from July to August, when the NAMA circulation is most strong, with the southern band decreasing (on average 7.1%). Finally, as the NAMA begins to weaken through September, the CIAM outflow at the southern band slowly resumes with an average outflow of 18.8% and a maximum of 89.0%. Comparison of Figure 5b with Figure 5e demonstrates that this seasonal trend in dominant eastern outflow latitude is not a consequence of seasonal change in initial cross-tropopause convection location: the percent of outflow at these northern latitudes (Figure 5b) is much greater than the percent of total initial cross-tropopause convection occurring at these latitudes (Figure 5c). CIAM outflow in the northeastern region contributes more than 20 times the amount of initial cross-tropopause convection at these latitudes by percent.

The location of this NAMA-dependent northeastern outflow region is likely a result of the interaction of the NAMA with the larger dynamics of the UTLS during summer. Specifically, the northern edge of the NAMA in general coincides with the subtropical jet (Okabe, 1995; Siu & Bowman, 2019). In fact, as the NAMA shifts northward across the season, the subtropical jet can merge with the polar jet across the northern US (Okabe, 1995). This shared boundary is visible in Figures 2c and 2d in which the monthly average Montgomery streamfunction for July and August at 370 K show the co-location of the NAMA with the jet between approximately 45°N and 55°N. Much of the outflow from the trajectories shown in Figures 2c and 2d, also occurs in this region.

The influence of the NAMA circulation on outflow over the western boundary is less apparent (Figure 5a). Throughout the entire time period studied, the majority of CIAM outflow across the western boundary occurs in the tropics (97.5% of total CIAM outflow along this boundary occurs below 30°N and 83.9% below 20°N) with little variability. It is important to note, however, that outflow across the western boundary does not occur before late May, and is sporadic until mid-June.

The seasonal dependence of the southwestern outflow region is more clearly shown in Figure 6, which depicts the percent contribution of each major outflow region (northeast, southeast, and southwest) to the total NAMA-influenced CIAM outflow across all boundaries as a function of time for selected isentropes. Figure 6a demonstrates that the southwest outflow region only begins to constitute greater than 10% of total outflow in late June, after which it contributes to outflow episodically reaching a maximum of 92.8% in late August and early September before declining. The seasonal trend of southwestern outflow, like outflow across the northeastern boundary, follows the development and seasonal strength of the NAMA. Figure 5d shows that when accounting for the initial cross-tropopause convection latitude distribution, the seasonal structure remains. This seasonal trend in Figure 6a is not visible in Figure 5a due to differences in normalization. In Figure 5a the outflow at each latitude is expressed as the percent of outflow across the western boundary rather than of all outflow across all boundaries as in Figure 6a. Figure 6b, however, shows that while outflow across the southwestern boundary is significant relative to all outflow in late June, large outflow does not occur across this boundary until late July and August in terms of numbers of CIAMs.

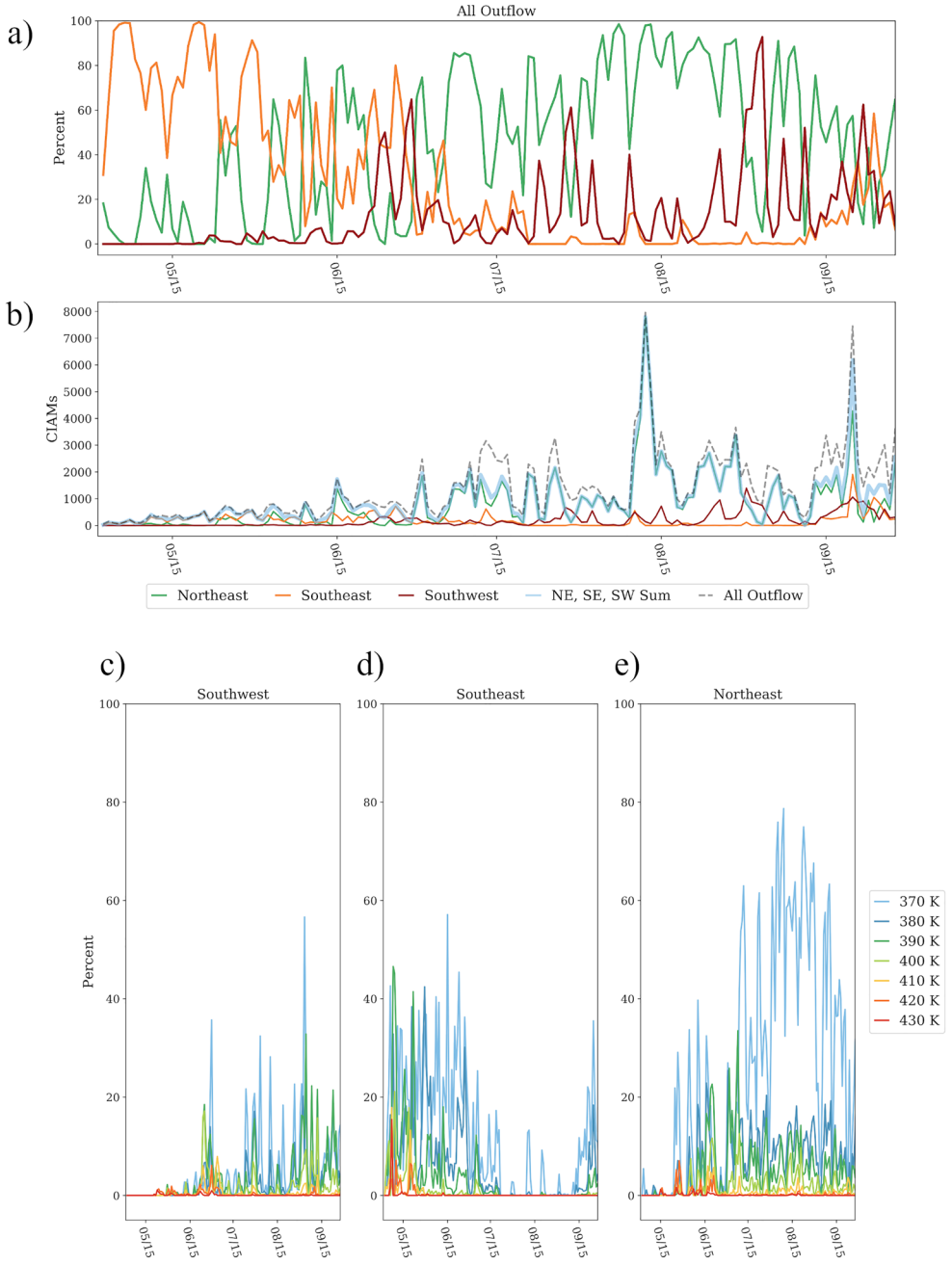

Figure 6. The seasonal changes in the contributions of each outflow region as a function of time at a daily resolution. Panel (a) shows the percent of total CIAM outflow through each outflow region (indicated by color) as a function of time. Panel (b) shows the absolute number of total CIAM outflow (gray dashed line), of the sum of the three identified outflow regions, and of each individual outflow region (indicated by color). Panels (c–e) show the relative contributions of CIAM outflow at different potential temperatures as a function of time for the southwest, southeast, and northeast outflow regions, respectively.

Figure 6 shows the contribution of the three major CIAM outflow regions (southwest, southeast, and northeast) as a percentage of total outflow and function of time for selected isentropes to determine if outflow had any altitude dependence. Here again we see the distribution of CIAM outflow between these three regions has a seasonal structure, determined by the presence and strength of the NAMA. In May when the NAMA is absent and the flow is predominantly zonal, the majority of CIAM outflow occurs in the southeast region, on average 75.5%. Similarly, without the presence of the NAMA circulation during this period, few

CIAMS exit through the southwest and northeast regions (on average 0.7% and 13.1% in May). In contrast, during July and August, when the NAMA is at its strongest, the southwest and northeast account for 13.4% and 68.1% of total CIAM outflow respectively, while the southeast contribution drops to 5.6%. CIAM outflow transitions between these regions through June as the NAMA forms. September is also a transition period as the NAMA weakens and outflow shifts away from the northeast and southwest region to the southeast region.

Figure 6b shows the absolute rate of daily CIAM total outflow as well as the contributions of each outflow region as a function of time. The number of CIAM outflow increases across the season with a maximum in August, following the seasonal trend of cross-tropopause convection, which also grows during the summer with a peak in August (Figure 4a). Of particular interest are the large outflow events occurring in early August and late September. Figures 1a and 1b show that the NAMA broadened significantly to the east around August 12 at both 370 and 400 K, and at 370 K the Montgomery potential gradient weakened to the east, likely resulting in an episode of large outflow. Similarly, around September 18 there is another eastward shift of the NAMA visible, though less pronounced as the NAMA is generally weaker in this period.

It is also evident in Figures 6c–6e, which show the percentage of CIAM outflow occurring at each outflow region within 10 K bins centered at the labeled potential temperatures, that much of the seasonal cycle in CIAM outflow is driven by the lower levels, that is, 370, 380, and 390 K. Outflow at 370 K accounts for the majority of the change in the distribution, with its contribution varying between 0% and 78.7% in any one given region. For comparison 380 K varies between 0% and 42.4%, and 400 K between 0% and 21.2%. This is expected as the number of CIAMs that reach upper levels is significantly lower, with the difference between 400 and 370 K being approximately an order of magnitude (Clapp et al., 2019). The seasonal shift of the dominant CIAM outflow region from the southeast prior to the NAMA, to the northeast and southwest during the NAMA's peak, to returning to the southeast as the NAMA weakens, however, is visible at all levels.

To quantify the overall impact of the NAMA circulation on meridional transport, Figure 7 shows the average change in latitude from trajectory initiation to outflow for each CIAM as a function of the initial OT time for selected isentropes for all outflow (Figure 7a), and subdivided for each outflow region (Figures 7b–7d). Figure 7a captures the seasonal effect of the NAMA on meridional transport of convective outflow over North America. In May and early June, prior to the NAMA's influence, there is little meridional displacement of CIAM trajectories (on average 3.3° northward in May). In July and August when the NAMA is strongest, however, CIAM trajectories on average move 24.5° northward. Finally, in September as the NAMA weakens, the meridional transport of CIAMs drops to 14.6° northward. These seasonal trends are largely consistent across all levels. The uppermost levels (410–430 K), however, experience greater variability compared to lower levels due to the smaller population of CIAMs at these heights (as can be seen in their absence at many time steps). Overall, the NAMA circulation results in a large-scale meridional displacement of convective outflow of up to ∼40° northward.

Not surprisingly, the meridional displacement of convective outflow is determined primarily by outflow region (Figures 7b–7d). For CIAMs exiting the northeast outflow region, the average northward change in latitude is 26.3° (Figure 7d). This is a direct result of the interaction between where cross-tropopause convection occurs, that is, the initial OT locations, and where the CIAMs are carried via the NAMA. This northward transport is only slightly offset by southward transport in the southwest outflow region with an average southward change in latitude of 6.9° (Figure 7b). Outflow in the southeast outflow region experiences little change in latitude with an average northward change in latitude of 4.2° (Figure 7c). The overall seasonal change (Figure 7a) is not as visible in the regionally subdivided outflow because the influence of the NAMA changes the proportion of CIAM outflow occurring in each region (as seen in Figure 6), not the magnitude of meridional transport occurring at each region. Evidence of the seasonal trend manifests as the absence of consistent outflow in the northeast and southwest regions before the NAMA develops, and as the decrease in consistent outflow in the southeast region during the height of the NAMA.

Cross-tropopause convection that occurs over North America has two distinct regions of eastward outflow, one to the north and one to the south, to the global stratosphere over the Atlantic that are dependent on the NAMA circulation. Prior to the development of the NAMA, CIAM outflow is dominated by a

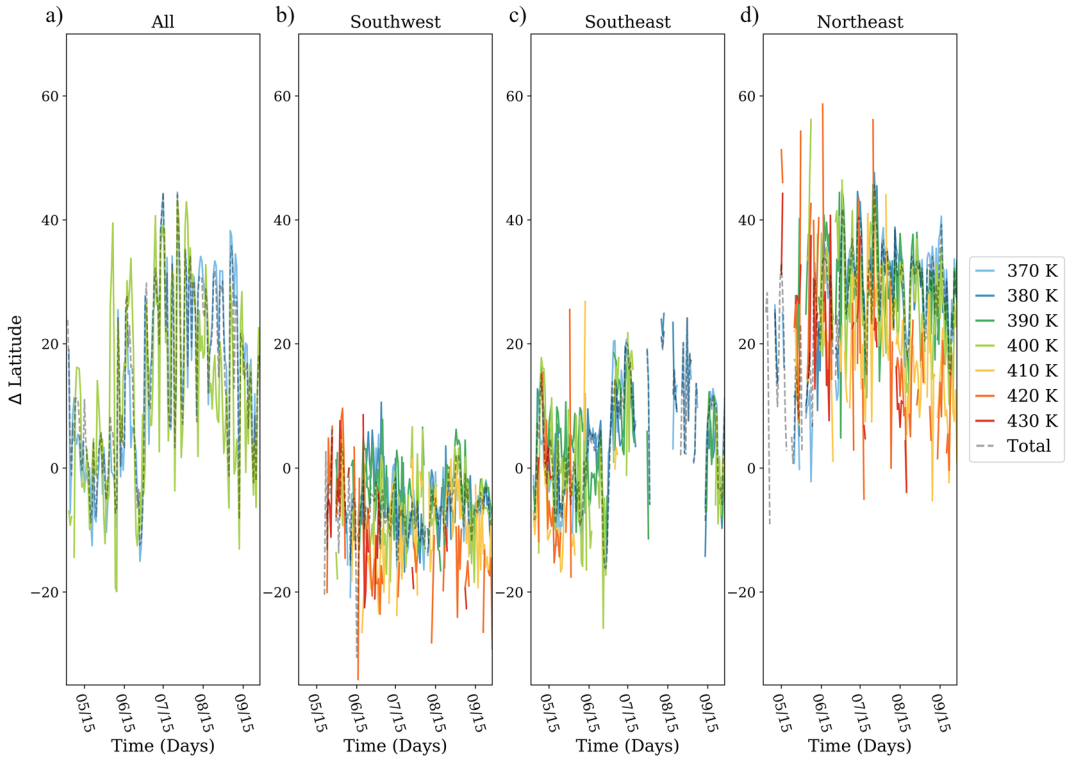

Figure 7. The seasonal dependence of the meridional transport of CIAMs mediated by the NAMA circulation. Panel (a) shows the average total change in latitude between CIAM initiation and outflow for all CIAMs as a function of time over all potential temperatures and at 370 and 400 K specifically. Outflow at 370 and 400 K specifically are selected to capture "lower" and "upper" level differences without losing clarity within the figure. Panels (b–d) depict the average total change in latitude across CIAM trajectories as a function of time for different potential temperatures and averaged over all levels for outflow in the southwest, southeast, and northeast outflow regions respectively.

tropical/sub-tropical southern band, while during the peak of the NAMA circulation CIAM outflow occurs in an extratropical northern band.

In order to determine if the NAMA-mediated meridional transport exhibited geographic biases, Figure 8 shows the average change in latitude from the initiation of the CIAM trajectory to the trajectory outflow for all CIAMs included in the study (as defined in the Methods section) binned in a 1° × 1° grid for August 2013 at 370 and 400 K. This figure illustrates the geographic distribution of meridional transport of CIAMs resulting from the NAMA circulation. There is a clear dependence of the magnitude of meridional displacement on the initial latitude of the CIAM with a strong overall northward transport trend. CIAMs initiated at lower latitudes experience greater displacement northward (on average 31.4° northward for those initiated 0°N-25°N) than those initiated in the subtropics (12.3° northward initiated 25°N-35°N) and midlatitudes (5.3° northward initiated 35°N-60°N) at 370 K. This is expected given that outflow of NAMA-influenced CIAMs occurs in the discrete outflow regions at the fixed latitudes identified earlier (see Figure 5). CIAMs caught in the southern edge of the NAMA circulation will experience greater northward transport to the northeast outflow region, which dominates outflow at the height of the NAMA (see Figure 6a) than CIAMs resulting from cross-tropopause convection in the central US for example.

Transport resulting from outflow in the southwest outflow region (the second significant outflow region when the NAMA is active) is visible in the midlatitudes. Southward displacement of a scattering of CIAMs initiated over the US (shown in green in Figure 8) is interspersed with northward displacement (shown in yellow in Figure 8). Further, differences in meridional transport of CIAMs between 370 and 400 K shows the vertical structure of the NAMA. As the center of the NAMA shifts northward at higher altitudes (see Figure 1), CIAMs initiated at the same latitude are displaced further north at 400 K than at 370 K. For example, CIAM trajectories initiated between 25°N and 35°N are transported on average 14.7° north at 400 K

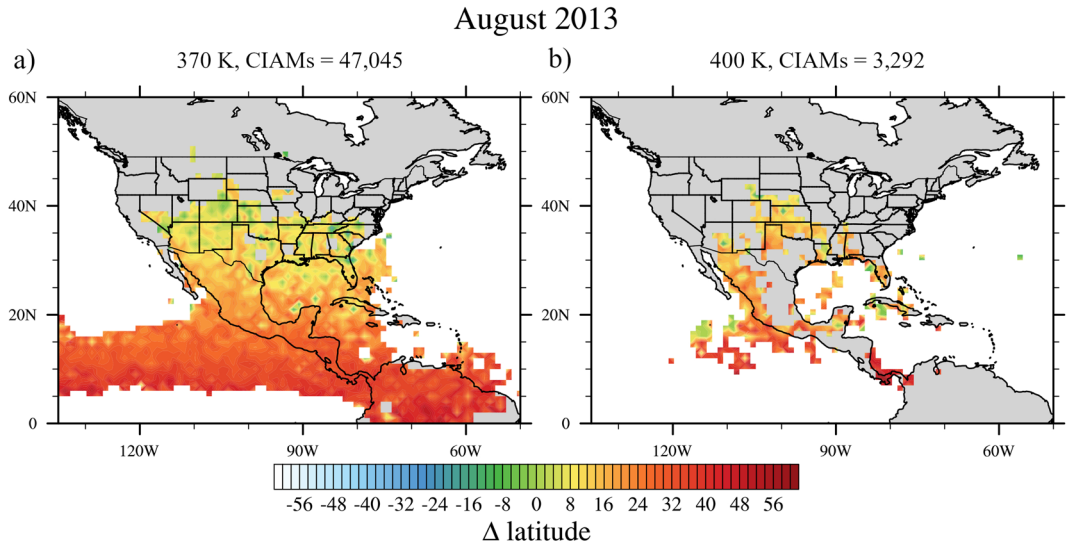

Figure 8. The geographic dependence of meridional transport of CIAMs during the month of August. The latitude displacements for all CIAMs initiated within each 1° × 1° bin throughout the month are averaged together such that the color contour indicates the average change in latitude a CIAM originating from that geographic position would encounter. The left panel shows the values for CIAMs at 370 K and the right panel for CIAMs at 400 K.

during August. The distribution of initial NAMA-influenced cross-tropopause convective events visible in Figure 8 follows the trends identified in Clapp et al. (2019) in which the tropics are the most significant contributor at lower levels while at upper levels convection occurring over the Sierra Madre Occidental and the central US dominate.

4. Conclusions

We identify two distinct outflow regions of CIAMs from the NAMA circulation using a trajectory analysis of cross-tropopause convection identified with GOES satellite imagery. The first outflow region is centered on the northeastern edge of the NAMA around 45°N and 45°W, and the second is centered on the southwestern edge around 10°N and 145°W. These outflow regions are seasonally dependent, concurrent with the development of the NAMA. Prior to the initiation of the NAMA circulation in May and early June, little to no CIAM outflow occurs in these regions, while during the height of the NAMA in July and August, 91.1% of all CIAMs outflow in these regions on average. Geographically static NAMA outflow regions result in significant meridional transport of CIAMs. In July and August, the average CIAM is transported 30.9°N in the northeast outflow region and 7.6°S in the southwest outflow region. Because more CIAMs are transported through the northeast outflow region, the average net meridional transport of CIAMs by the NAMA circulation is 22.0°N in July and August. This meridional transport is largely altitude independent, although the majority of outflow occurs at lower levels as expected given the altitude distribution of initial cross-tropopause convection.

This development of two primary outflow regions from the NAMA (northeast and southwest) is similar to the two eastern and western horizontal transport pathways from the Asian monsoon to the global stratosphere resulting from eddy shedding (e.g., Fadnavis et al., 2018; Garny & Randel, 2016; Vogel, Günther, Müller, Grooß, Afchine, et al., 2016). Moreover, Vogel, Günther, Müller, Grooß, Afchine, et al. (2016) also found a north-south bias in outflow from the Asian monsoon anticyclone (AMA) such that the eastward transport occurred along the northern edge of the monsoon circulation and the westward transport occurred along the southern edge. The position of the northeastern outflow from the AMA was also determined by the boundary between the monsoon anticyclone and the subtropical jet (Vogel, Günther, Müller, Grooß, Afchine, et al., 2016). Future work should probe these similarities in transport and outflow from upper level monsoon anticyclones, including an investigation into how the relative intermittency and weakness of the

NAMA compared to the AMA influences the structure of outflow, especially with regards to the episodic nature of NAMA outflow.

In our analysis, we chose a study region representative of the NAMA that was larger than the instantaneous geographic extent of the NAMA (as defined by a closed contour of the Montgomery streamfunction at any given potential temperature level) to account for the instability of the NAMA in both position and strength. Using a larger representative region ensured consideration of all CIAMs likely influenced by the anticyclonic circulation. The seasonal differences in the advection and outflow of CIAMs reveal the shift from a largely westerly zonal flow in the ULTS to a UTLS influenced by the NAMA. The circulation of all CIAMs within the study region, however, cannot be solely attributed to the effects of the NAMA given its variability. Further, our analysis is limited to 2013 and therefore does not capture potential interannual variability present in both the distribution and frequency of cross-tropopause convection and the position and strength of the NAMA. Conclusions drawn from one year of data are also susceptible to extreme events within the highly episodic NAMA outflow, which could introduce atypical trends that are not consistent interannually. Expanding the analysis to include additional years would allow for an investigation of interannual variability, an improvement of regional definitions, and an examination of the episodic nature of NAMA outflow seen in 2013 to determine if it is a regular feature and identify its cause. Similarly, extending the analysis through October would allow for an evaluation of the dissipation of the NAMA.

Previous work has studied the importance of vertical transport and subsequent meridional advection of air masses within the summer monsoon regions in the northern hemisphere. This research has demonstrated the role of the summer monsoons in moistening the global lower stratosphere (Nützel et al., 2019; Ploeger, Günther, et al., 2013; Poshyvailo et al., 2018) as well as transporting other trace species and pollution into the stratosphere (Ploeger, Konopka, et al., 2017). While these studies conclude that the Asian monsoon's influence on the lower stratosphere is much more significant than the North American monsoon's influence, they do not consider the influence of cross-tropopause convection. Further, though they accurately recreate the water vapor maximum over the Asian monsoon, they do not capture the full magnitude or geographic distribution of the water vapor maximum over the North American monsoon. This may result from the potential for cross-tropopause convection to contribute as much as 45% of the stratospheric water vapor over North America, which has been estimated from HDO observations (Hanisco et al., 2007).

Relative to the Asian monsoon, however, convection over North America more frequently crosses the tropopause due to differences in both tropopause height and the altitudes reached by convection (Jensen et al., 2020). As a result, the majority of MLS-observed water vapor enhancements over the North America, including the North American monsoon, occur above the tropopause, in contrast to the Asian monsoon where 90% of high water vapor values occur below the cold-point tropopause, indicating the importance of direct convective hydration of the lower stratosphere over North America (Jensen et al., 2020). Furthermore, Yu et al. (2020) find that the boreal summer deep convection occurring over the contiguous US alone, as observed by NEXRAD radar, moistens the lower stratosphere over North America by approximately 1 ppmv.

In this study, we directly address the impact of NAMA-mediated meridional transport on cross-tropopause convection. We show that the northward meridional transport of convectively influenced air in the lower stratosphere is common within the NAMA using a trajectory analysis applied to a climatology of cross-tropopause convection. Further, we have identified the dominant outflow regions of CIAMs that indicate the importance of isentropic transport seen in prior studies (Kunz et al., 2015; Pittman et al., 2007). This transport of CIAMs through the NAMA has implications for assessing the impact of cross-tropopause convection over North America on the global stratospheric water budget, as well as the transport of tropospheric trace gases including VSLS and pollutants from this region that could impact the chemistry and ozone of the lower stratosphere globally. In particular, given that the NAMA transports CIAMs on average 22.0° northward, cross-tropopause convection occurring over the Sierra Madres and within the southern edge of the NAMA should be considered.

This study, however, does not attempt to quantify the effect of cross-tropopause convective transport and subsequent meridional advection through the NAMA in part because the GOES data used to construct the climatology is sufficient to capture seasonal trends and geographic distributions, but is not a complete

budget. As such it is complementary to the work done using NEXRAD-derived GridRad data (Cooney et al., 2018; Yu et al., 2020), which provides a more complete record of cross-tropopause convection, but is limited in scope to the continental US. Future work seeking to quantify the total influence of all cross-tropopause convection occurring within the North American monsoon region on the lower stratosphere must consider the effects of the northward meridional transport of convective outflow by the NAMA.

Conflict of Interest

The authors declare no conflicts of interest relevant to this study.

Data Availability Statement

The GOES-OT/CIAM trajectory files are available for download at https://dataverse.harvard.edu/dataset.xhtml?persistentId=doi:10.7910/DVN/DBU42P. MERRA-2 reanalysis data is available for download at https://disc.gsfc.nasa.gov/datasets?project=MERRA-2. GOES-13,15 4-km IRW BT and 1-km VIS data (available for download at https://www.avl.class.noaa.gov/saa/products/search?datatype_family=GVAR_IMG) were used to generate OT detections.

Acknowledgments
The authors would like to thank the members of the Anderson group for their support. This work has been supported by the National Aeronautics and Space Administration (NASA) under NASA award numbers NNX15AF60G (UV Absorption Cross Sections and Equilibrium Constant of ClOOCl Determined from New Laboratory Spectroscopy Studies of ClOOCl and ClO) and a grant from the National Science Foundation (NSF) Arctic Observing Network (AON) Program under NSF award number 1203583 (Collaborative Research: Multi-Regional Scale Aircraft Observations of Methane and Carbon Dioxide Isotopic Fluxes in the Arctic).

References

Anderson, J. G., & Clapp, C. E. (2018). Coupling free radical catalysis, climate change, and human health. *Physical Chemistry Chemical Physics*, *20*(16), 10569–10587. https://doi.org/10.1039/c7cp08331a

Anderson, J. G., Weisenstein, D. K., Bowman, K. P., Homeyer, C. R., Smith, J. B., Wilmouth, D. M., et al. (2017). Stratospheric ozone over the United States in summer linked to observations of convection and temperature via chlorine and bromine catalysis. *Proceedings of the National Academy of Sciences*, *114*(25), E4905–E4913. https://doi.org/10.1073/pnas.1619318114

Anderson, J. G., Wilmouth, D. M., Smith, J. B., & Sayres, D. S. (2012). UV dosage levels in summer: Increased risk of ozone loss from convectively injected water vapor. *Science*, *337*(6096), 835–839. https://doi.org/10.1126/science.1222978

Bedka, K. M., & Khlopenkov, K. (2016). A probabilistic multispectral pattern recognition method for detection of overshooting cloud tops using passive satellite imager observations. *Journal of Applied Meteorology and Climatology*, *55*(9), 1983–2005. https://doi.org/10.1175/jamc-d-15-0249.1

Bowman, K. P., Lin, J. C., Stohl, A., Draxler, R., Konopka, P., Andrews, A., & Brunner, D. (2013). Input data requirements for Lagrangian trajectory models. *Bulletin of the American Meteorological Society*, *94*(7), 1051–1058. https://doi.org/10.1175/bams-d-12-00076.1

Bucci, S., Legras, B., Sellitto, P., D'Amato, F., Viciani, S., Montori, A., et al. (2020). Deep-convective influence on the upper troposphere-lower stratosphere composition in the Asian monsoon anticyclone region: 2017 StratoClim campaign results. *Atmospheric Chemistry and Physics*, *20*(20), 12193–12210. https://doi.org/10.5194/acp-20-12193-2020

Clapp, C. E., Smith, J. B., Bedka, K. M., & Anderson, J. G. (2019). Identifying source regions and the distribution of cross-tropopause convective outflow over North America during the warm season. *Journal of Geophysical Research: Atmospheres*, *124*(24), 13750–13762. https://doi.org/10.1029/2019JD031382

Cooney, J. W., Bowman, K. P., Homeyer, C. R., & Fenske, T. M. (2018). Ten year analysis of tropopause-overshooting convection using GridRad data. *Journal of Geophysical Research: Atmospheres*, *123*(1), 329–343. https://doi.org/10.1002/2017JD027718

Corti, T., Luo, B. P., de Reus, M., Brunner, D., Cairo, F., Mahoney, M. J., et al. (2008). Unprecedented evidence for deep convection hydrating the tropical stratosphere. *Geophysical Research Letters*, *35*(10), L10810. https://doi.org/10.1029/2008GL033641

de Reus, M., Borrmann, S., Bansemer, A., Heymsfield, A. J., Weigel, R., Schiller, C., et al. (2009). Evidence for ice particles in the tropical stratosphere from in-situ measurements. *Atmospheric Chemistry and Physics*, *9*(18), 6775–6792. https://doi.org/10.5194/acp-9-6775-2009

Diem, J. E., Brown, D. P., & McCann, J. (2013). Multi-decadal changes in the North American monsoon anticyclone. *International Journal of Climatology*, *33*(9), 2274–2279. https://doi.org/10.1002/joc.3576

Eguchi, N., Kodera, K., Funatsu, B. M., Takashima, H., & Ueyama, R. (2016). Rapid convective transport of tropospheric air into the tropical lower stratosphere during the 2010 sudden stratospheric warming. *Sola*, *12A*, 13–17. https://doi.org/10.2151/sola.12A-003

Fadnavis, S., Roy, C., Chattopadhyay, R., Sioris, C. E., Rap, A., Müller, R., et al. (2018). Transport of trace gases via eddy shedding from the Asian summer monsoon anticyclone and associated impacts on ozone heating rates. *Atmospheric Chemistry and Physics*, *18*(15), 11493–11506. https://doi.org/10.5194/acp-18-11493-2018

Fiehn, A., Quack, B., Hepach, H., Fuhlbrügge, S., Tegtmeier, S., Toohey, M., et al. (2017). Delivery of halogenated very short-lived substances from the west Indian Ocean to the stratosphere during the Asian summer monsoon. *Atmospheric Chemistry and Physics*, *17*(11), 6723–6741. https://doi.org/10.5194/acp-17-6723-2017

Frey, W., Schofield, R., Hoor, P., Kunkel, D., Ravegnani, F., Ulanovsky, A., et al. (2015). The impact of overshooting deep convection on local transport and mixing in the tropical upper troposphere/lower stratosphere (UTLS). *Atmospheric Chemistry and Physics*, *15*(11), 6467–6486. https://doi.org/10.5194/acp-15-6467-2015

Garny, H., & Randel, W. J. (2016). Transport pathways from the Asian monsoon anticyclone to the stratosphere. *Atmospheric Chemistry and Physics*, *16*(4), 2703–2718. https://doi.org/10.5194/acp-16-2703-2016

Geil, K. L., Serra, Y. L., & Zeng, X. (2013). Assessment of CMIP5 model simulations of the North American monsoon system. *Journal of Climate*, *26*(22), 8787–8801. https://doi.org/10.1175/jcli-d-13-00044.1

Gelaro, R., McCarty, W., Suárez, M. J., Todling, R., Molod, A., Takacs, L., et al. (2017). The modern-era retrospective analysis for research and applications, version 2 (MERRA-2). *Journal of Climate*, *30*(14), 5419–5454. https://doi.org/10.1175/jcli-d-16-0758.1

Gettelman, A., Kinnison, D. E., Dunkerton, T. J., & Guy, B. P. (2004). Impact of monsoon circulations on the upper troposphere and lower stratosphere. *Journal of Geophysical Research*, *109*(D22), D22101. https://doi.org/10.1029/2004jd004878

Griffin, S. M., Bedka, K. M., & Velden, C. S. (2016). A method for calculating the height of overshooting convective cloud tops using satellite-based IR imager and CloudSat cloud profiling radar observations. *Journal of Applied Meteorology and Climatology*, *55*(2), 479–491. https://doi.org/10.1175/jamc-d-15-0170.1

Hanisco, T. F., Moyer, E. J., Weinstock, E. M., St. Clair, J. M., Sayres, D. S., Smith, J. B., et al. (2007). Observations of deep convective influence on stratospheric water vapor and its isotopic composition. *Geophysical Research Letters*, *34*(4), L04814. https://doi.org/10.1029/2006GL027899

Hassim, M. E. E., & Lane, T. P. (2010). A model study on the influence of overshooting convection on TTL water vapour. *Atmospheric Chemistry and Physics*, *10*(20), 9833–9849. https://doi.org/10.5194/acp-10-9833-2010

Hegglin, M. I., Brunner, D., Wernli, H., Schwierz, C., Martius, O., Hoor, P., et al. (2004). Tracing troposphere-to-stratosphere transport above a mid-latitude deep convective system. *Atmospheric Chemistry and Physics*, *4*(3), 741–756. https://doi.org/10.5194/acp-4-741-2004

Herman, R. L., Ray, E. A., Rosenlof, K. H., Bedka, K. M., Schwartz, M. J., Read, W. G., et al. (2017). Enhanced stratospheric water vapor over the summertime continental United States and the role of overshooting convection. *Atmospheric Chemistry and Physics*, *17*(9), 6113–6124. https://doi.org/10.5194/acp-17-6113-2017

Hoffmann, L., Günther, G., Li, D., Stein, O., Wu, X., Griessbach, S., et al. (2019). From ERA-Interim to ERA5: The considerable impact of ECMWF's next-generation reanalysis on Lagrangian transport simulations. *Atmospheric Chemistry and Physics*, *19*(5), 3097–3124. https://doi.org/10.5194/acp-19-3097-2019

Homeyer, C. R. (2014). Formation of the enhanced-V infrared cloud-top feature from high-resolution three-dimensional radar observations. *Journal of the Atmospheric Sciences*, *71*(1), 332–348. https://doi.org/10.1175/jas-d-13-079.1

Homeyer, C. R., McAuliffe, J. D., & Bedka, K. M. (2017). On the development of above-anvil cirrus plumes in extratropical convection. *Journal of the Atmospheric Sciences*, *74*(5), 1617–1633. https://doi.org/10.1175/JAS-D-16-0269.1

Iwasaki, S., Shibata, T., Nakamoto, J., Okamoto, H., Ishimoto, H., & Kubota, H. (2010). Characteristics of deep convection measured by using the A-train constellation. *Journal of Geophysical Research*, *115*(D6), D06207. https://doi.org/10.1029/2009JD013000

Iwasaki, S., Shibata, T., Okamoto, H., Ishimoto, H., & Kubota, H. (2012). Mixtures of stratospheric and overshooting air measured using A-Train sensors. *Journal of Geophysical Research*, *117*(D12), D12207. https://doi.org/10.1029/2011jd017402

Jensen, E. J., Pan, L. L., Honomichl, S., Diskin, G. S., Krämer, M., Spelten, N., et al. (2020). Assessment of observational evidence for direct convective hydration of the lower stratosphere. *Journal of Geophysical Research: Atmospheres*, *125*(15), e2020JD032793. https://doi.org/10.1029/2020JD032793

Khaykin, S., Pommereau, J.-P., Korshunov, L., Yushkov, V., Nielsen, J., Larsen, N., et al. (2009). Hydration of the lower stratosphere by ice crystal geysers over land convective systems. *Atmospheric Chemistry and Physics*, *9*(6), 2275–2287. https://doi.org/10.5194/acp-9-2275-2009

Khaykin, S. M., Pommereau, J.-P., Riviere, E. D., Held, G., Ploeger, F., Ghysels, M., et al. (2016). Evidence of horizontal and vertical transport of water in the Southern Hemisphere tropical tropopause layer (TTL) from high-resolution balloon observations. *Atmospheric Chemistry and Physics*, *16*(18), 12273–12286. https://doi.org/10.5194/acp-16-12273-2016

Kuilman, M. S., Zhang, Q., Cai, M., & Wen, Q. (2020). Using the climate feedback response analysis method to quantify climate feedbacks in the middle atmosphere. *Atmospheric Chemistry and Physics*, *20*(21), 12409–12430. https://doi.org/10.5194/acp-20-12409-2020

Kunz, A., Sprenger, M., & Wernli, H. (2015). Climatology of potential vorticity streamers and associated isentropic transport pathways across PV gradient barriers. *Journal of Geophysical Research: Atmospheres*, *120*(9), 3802–3821. https://doi.org/10.1002/2014jd022615

Li, Q., Jacob, D. J., Park, R., Wang, Y., Heald, C. L., Hudman, R., et al. (2005). North American pollution outflow and the trapping of convectively lifted pollution by upper-level anticyclone. *Journal of Geophysical Research*, *110*(D10), D10301. https://doi.org/10.1029/2004jd005039

Liang, Q., Atlas, E., Blake, D., Dorf, M., Pfeilsticker, K., & Schauffler, S. (2014). Convective transport of very short lived bromocarbons to the stratosphere. *Atmospheric Chemistry and Physics*, *14*(11), 5781–5792. https://doi.org/10.5194/acp-14-5781-2014

Nowack, P. J., Abraham, N. L., Braesicke, P., & Pyle, J. A. (2018). The impact of stratospheric ozone feedbacks on climate sensitivity estimates. *Journal of Geophysical Research: Atmospheres*, *123*(9), 4630–4641. https://doi.org/10.1002/2017JD027943

Nützel, M., Podglajen, A., Garny, H., & Ploeger, F. (2019). Quantification of water vapour transport from the Asian monsoon to the stratosphere. *Atmospheric Chemistry and Physics*, *19*(13), 8947–8966. https://doi.org/10.5194/acp-19-8947-2019

Okabe, I. T. (1995). *The North American monsoon* (Doctoral dissertation). University of British Columbia. UBC Theses and Dissertations. Retrieved from hdl.handle.net/2429/8953

Phoenix, D. B., Homeyer, C. R., & Barth, M. C. (2017). Sensitivity of simulated convection-driven stratosphere-troposphere exchange in WRF-Chem to the choice of physical and chemical parameterization. *Earth and Space Science*, *4*(8), 454–471. https://doi.org/10.1002/2017ea000287

Phoenix, D. B., Homeyer, C. R., Barth, M. C., & Trier, S. B. (2020). Mechanisms responsible for stratosphere-to-troposphere transport around a mesoscale convective system anvil. *Journal of Geophysical Research: Atmospheres*, *125*(10), e2019JD032016. https://doi.org/10.1029/2019jd032016

Pittman, J. V., Weinstock, E. M., Oglesby, R. J., Sayres, D. S., Smith, J. B., Anderson, J. G., et al. (2007). Transport in the subtropical lowermost stratosphere during the Cirrus Regional Study of Tropical Anvils and Cirrus Layers–Florida Area Cirrus Experiment. *Journal of Geophysical Research: Atmospheres*, *112*(D8). https://doi.org/10.1029/2006jd007851

Ploeger, F., Gottschling, C., Griessbach, S., Grooß, J.-U., Guenther, G., Konopka, P., et al. (2015). A potential vorticity-based determination of the transport barrier in the Asian summer monsoon anticyclone. *Atmospheric Chemistry and Physics*, *15*(22), 13145–13159. https://doi.org/10.5194/acp-15-13145-2015

Ploeger, F., Günther, G., Konopka, P., Fueglistaler, S., Müller, R., Hoppe, C., et al. (2013). Horizontal water vapor transport in the lower stratosphere from subtropics to high latitudes during boreal summer. *Journal of Geophysical Research: Atmospheres*, *118*(14), 8111–8127. https://doi.org/10.1002/jgrd.50636

Ploeger, F., Konopka, P., Walker, K., & Riese, M. (2017). Quantifying pollution transport from the Asian monsoon anticyclone into the lower stratosphere. *Atmospheric Chemistry and Physics*, *17*(11), 7055–7066. https://doi.org/10.5194/acp-17-7055-2017

Popovic, J. M., & Plumb, R. A. (2001). Eddy shedding from the upper-tropospheric Asian monsoon anticyclone. *Journal of the Atmospheric Sciences*, *58*(1), 93–104. https://doi.org/10.1175/1520-0469(2001)058<0093:esftut>2.0.co;2

Poshyvailo, L., Müller, R., Konopka, P., Günther, G., Riese, M., Podglajen, A., & Ploeger, F. (2018). Sensitivities of modelled water vapour in the lower stratosphere: Temperature uncertainty, effects of horizontal transport and small-scale mixing. *Atmospheric Chemistry and Physics*, *18*(12), 8505–8527. https://doi.org/10.5194/acp-18-8505-2018

Poulida, O., Dickerson, R. R., & Heymsfield, A. (1996). Stratosphere-troposphere exchange in a midlatitude mesoscale convective complex: 1. Observations. *Journal of Geophysical Research*, *101*(D3), 6823–6836. https://doi.org/10.1029/95jd03523

Qu, Z., Huang, Y., Vaillancourt, P. A., Cole, J. N. S., Milbrandt, J. A., Yau, M.-K., et al. (2020). Simulation of convective moistening of the extratropical lower stratosphere using a numerical weather prediction model. *Atmospheric Chemistry and Physics*, *20*(4), 2143–2159. https://doi.org/10.5194/acp-20-2143-2020

Randel, W. J., Moyer, E., Park, M., Jensen, E., Bernath, P., Walker, K., & Boone, C. (2012). Global variations of HDO and HDO/H_2O ratios in the upper troposphere and lower stratosphere derived from ACE-FTS satellite measurements. *Journal of Geophysical Research*, *117*(D6), D06303. https://doi.org/10.1029/2011JD016632

Randel, W. J., Zhang, K., & Fu, R. (2015). What controls stratospheric water vapor in the NH summer monsoon regions? *Journal of Geophysical Research: Atmospheres*, *120*(15), 7988–8001. https://doi.org/10.1002/2015jd023622

Ray, E. A., Rosenlof, K. H., Richard, E. C., Hudson, P. K., Cziczo, D. J., Loewenstein, M., et al. (2004). Evidence of the effect of summertime midlatitude convection on the subtropical lower stratosphere from CRYSTAL-FACE tracer measurements. *Journal of Geophysical Research*, *109*(D18), D18304. https://doi.org/10.1029/2004JD004655

Riese, M., Ploeger, F., Rap, A., Vogel, B., Konopka, P., Dameris, M., & Forster, P. (2012). Impact of uncertainties in atmospheric mixing on simulated UTLS composition and related radiative effects. *Journal of Geophysical Research*, *117*(D16). https://doi.org/10.1029/2012jd017751

Robrecht, S., Vogel, B., Grooß, J.-U., Rosenlof, K., Thornberry, T., Rollins, A., et al. (2019). Mechanism of ozone loss under enhanced water vapour conditions in the mid-latitude lower stratosphere in summer. *Atmospheric Chemistry and Physics*, *19*(9), 5805–5833. https://doi.org/10.5194/acp-19-5805-2019

Sang, W., Huang, Q., Tian, W., Wright, J. S., Zhang, J., Tian, H., et al. (2018). A large eddy model study on the effect of overshooting convection on lower stratospheric water vapor. *Journal of Geophysical Research: Atmospheres*, *123*(18), 10023–10038. https://doi.org/10.1029/2017jd028069

Santee, M. L., Manney, G. L., Livesey, N. J., Schwartz, M. J., Neu, J. L., & Read, W. G. (2017). A comprehensive overview of the climatological composition of the Asian summer monsoon anticyclone based on 10 years of Aura Microwave Limb Sounder measurements. *Journal of Geophysical Research: Atmospheres*, *122*(10), 5491–5514. https://doi.org/10.1002/2016jd026408

Sargent, M. R., Smith, J. B., Sayres, D. S., & Anderson, J. G. (2014). The roles of deep convection and extratropical mixing in the tropical tropopause layer: An in situ measurement perspective. *Journal of Geophysical Research: Atmospheres*, *119*(21), 355–412. https://doi.org/10.1002/2014JD022157

Sayres, D. S., Pfister, L., Hanisco, T. F., Moyer, E. J., Smith, J. B., St. Clair, J. M., et al. (2010). Influence of convection on the water isotopic composition of the tropical tropopause layer and tropical stratosphere. *Journal of Geophysical Research*, *115*(D10), D00J20. https://doi.org/10.1029/2009JD013100

Schoeberl, M. R., Pfister, L., Wang, T., Kummer, J., Dessler, A. E., & Yu, W. (2020). Erythemal radiation, column ozone, and the North American monsoon. *Journal of Geophysical Research: Atmospheres*, *125*(19), e2019JD032283. https://doi.org/10.1029/2019jd032283

Schwartz, M. J., Read, W. G., Santee, M. L., Livesey, N. J., Froidevaux, L., Lambert, A., & Manney, G. L. (2013). Convectively injected water vapor in the North American summer lowermost stratosphere. *Geophysical Research Letters*, *40*(10), 2316–2321. https://doi.org/10.1002/grl.50421

Shine, K. P., Bourqui, M. S., Forster, P. M. de F., Hare, S. H. E., Langematz, U., Braesicke, P., et al. (2003). A comparison of model-simulated trends in stratospheric temperatures. *Quarterly Journal of the Royal Meteorological Society*, *129*(590), 1565–1588. https://doi.org/10.1256/qj.02.186

Sinnhuber, B.-M., & Meul, S. (2015). Simulating the impact of emissions of brominated very short lived substances on past stratospheric ozone trends. *Geophysical Research Letters*, *42*(7), 2449–2456. https://doi.org/10.1002/2014gl062975

Siu, L. W., & Bowman, K. P. (2019). Forcing of the upper-tropospheric monsoon anticyclones. *Journal of the Atmospheric Sciences*, *76*(7), 1937–1954. https://doi.org/10.1175/jas-d-18-0340.1

Smith, J. B., Wilmouth, D. M., Bedka, K. M., Bowman, K. P., Homeyer, C. R., Dykema, J. A., et al. (2017). A case study of convectively sourced water vapor observed in the overworld stratosphere over the United States. *Journal of Geophysical Research: Atmospheres*, *122*(17), 9529–9554. https://doi.org/10.1002/2017JD026831

Solomon, S., Kinnison, D., Garcia, R. R., Bandoro, J., Mills, M., Wilka, C., et al. (2016). Monsoon circulations and tropical heterogeneous chlorine chemistry in the stratosphere. *Geophysical Research Letters*, *43*(24), 12–624. https://doi.org/10.1002/2016gl071778

Solomon, S., Rosenlof, K. H., Portmann, R. W., Daniel, J. S., Davis, S. M., Sanford, T. J., & Plattner, G.-K. (2010). Contributions of stratospheric water vapor to decadal changes in the rate of global warming. *Science*, *327*(5970), 1219–1223. https://doi.org/10.1126/science.1182488

Stohl, A., Wotawa, G., Seibert, P., & Kromp-Kolb, H. (1995). Interpolation errors in wind fields as a function of spatial and temporal resolution and their impact on different types of kinematic trajectories. *Journal of Applied Meteorology*, *34*(10), 2149–2165. https://doi.org/10.1175/1520-0450(1995)034<2149:ieiwfa>2.0.co;2

Vera, C., Higgins, W., Amador, J., Ambrizzi, T., Garreaud, R., Gochis, D., et al. (2006). Toward a unified view of the American monsoon systems. *Journal of Climate*, *19*(20), 4977–5000. https://doi.org/10.1175/jcli3896.1

Vogel, B., Günther, G., Müller, R., Grooß, J.-U., Afchine, A., Bozem, H., et al. (2016). Long-range transport pathways of tropospheric source gases originating in Asia into the northern lower stratosphere during the Asian monsoon season 2012. *Atmospheric Chemistry and Physics*, *16*(23), 15301–15325. https://doi.org/10.5194/acp-16-15301-2016

Vogel, B., Günther, G., Müller, R., Grooß, J.-U., Hoor, P., Krämer, M., et al. (2014). Fast transport from Southeast Asia boundary layer sources to northern Europe: Rapid uplift in typhoons and eastward eddy shedding of the Asian monsoon anticyclone. *Atmospheric Chemistry and Physics*, *14*(23), 12745–12762. https://doi.org/10.5194/acp-14-12745-2014

Vogel, B., Müller, R., Günther, G., Spang, R., Hanumanthu, S., Li, D., et al. (2019). Lagrangian simulations of the transport of young air masses to the top of the Asian monsoon anticyclone and into the tropical pipe. *Atmospheric Chemistry and Physics*, *19*(9), 6007–6034. https://doi.org/10.5194/acp-19-6007-2019

Wales, P. A., Salawitch, R. J., Nicely, J. M., Anderson, D. C., Canty, T. P., Baidar, S., et al. (2018). Stratospheric injection of brominated very short-lived substances: Aircraft observations in the Western Pacific and representation in global models. *Journal of Geophysical Research: Atmospheres*, *123*(10), 5690–5719. https://doi.org/10.1029/2017jd027978

Wang, P. K., Su, S.-H., Charvát, Z., Štástka, J., & Lin, H.-M. (2011). Cross tropopause transport of water by mid-latitude deep convective storms: A review. *Terrestrial, Atmospheric and Oceanic Sciences*, *22*(5), 447–462. https://doi.org/10.3319/tao.2011.06.13.01(a)

Wang, X., Randel, W., & Wu, Y. (2021). Infrequent, rapid transport pathways to the summer North American upper troposphere and lower stratosphere. *Geophysical Research Letters*, *48*, e2020GL089763. https://doi.org/10.1029/2020gl089763

Weinstock, E. M., Pittman, J. V., Sayres, D. S., Smith, J. B., Anderson, J. G., Wofsy, S. C., et al. (2007). Quantifying the impact of the North American monsoon and deep midlatitude convection on the subtropical lowermost stratosphere using in situ measurements. *Journal of Geophysical Research*, *112*(D18), D18310. https://doi.org/10.1029/2007JD008554

Werner, F., Schwartz, M. J., Livesey, N. J., Read, W. G., & Santee, M. L. (2020). Extreme outliers in lower stratospheric water vapor over North America observed by MLS: Relation to overshooting convection diagnosed from colocated aqua-MODIS data. *Geophysical Research Letters*, *47*(24), e2020GL090131. https://doi.org/10.1029/2020GL090131

Wu, Y., Orbe, C., Tilmes, S., Abalos, M., & Wang, X. (2020). Fast transport pathways into the Northern Hemisphere upper troposphere and lower stratosphere during northern summer. *Journal of Geophysical Research: Atmospheres*, *125*(3), e2019JD031552. https://doi.org/10.1029/2019JD031552

Xia, Y., Huang, Y., & Hu, Y. (2018). On the climate impacts of upper tropospheric and lower stratospheric ozone. *Journal of Geophysical Research: Atmospheres*, *123*(2), 730–739. https://doi.org/10.1002/2017JD027398

Yan, X., Konopka, P., Ploeger, F., Podglajen, A., Wright, J. S., Müller, R., & Riese, M. (2019). The efficiency of transport into the stratosphere via the Asian and North American summer monsoon circulations. *Atmospheric Chemistry and Physics*, *19*(24), 15629–15649. https://doi.org/10.5194/acp-19-15629-2019

Yu, W., Dessler, A. E., Park, M., & Jensen, E. J. (2020). Influence of convection on stratospheric water vapor in the North American monsoon region. *Atmospheric Chemistry and Physics*, *20*(20), 12153–12161. https://doi.org/10.5194/acp-20-12153-2020